Practical test mass and suspension configuration for a cryogenic kilohertz gravitational wave detector

J. Eichholz,[1,*] N. A. Holland,[1] V. B. Adya,[1] J. V. van Heijningen,[2] R. L. Ward,[1] B. J. J. Slagmolen,[1] D. E. McClelland,[1] and D. J. Ottaway[3]

[1]*OzGrav-ANU, Centre for Gravitational Astrophysics, College of Science, The Australian National University, Acton, ACT 2601, Australia*

[2]*OzGrav-UWA, Department of Physics, University of Western Australia, Crawley, Western Australia 6009, Australia*

[3]*OzGrav-UoA, Department of Physics and the Institute of Photonics and Advanced Sensing (IPAS), University of Adelaide, Adelaide, South Australia 5005, Australia*

(Received 19 August 2020; accepted 21 October 2020; published 18 December 2020)

Designs for future gravitational wave detection facilities feature silicon test masses at cryogenic temperatures to reduce thermal noise and thermally induced aberrations. Designers call for operation at 123 K or close to 18 K to exploit the vanishing thermal expansion of crystalline silicon. The amount of absorbed heat that can be radiatively removed from the test masses is limited at these temperatures, forcing complex cooling scenarios to be considered, including conduction through suspension wires. This is particularly relevant for the kilohertz class of detectors that aim for extremely high circulating power, i.e., roughly a factor 20 more than the world record at the time of writing, to reduce quantum noise. We explore the impact of raising the test mass temperature and show that a dedicated kilohertz-band cryogenic instrument can do so without significant sensitivity penalty, thereby boosting the radiative cooling rate and allowing higher power operation with simpler suspensions. We also explore the implications of operating cryogenic broadband detectors at elevated temperatures. The work presented here was instrumental in the development of the Neutron Star Extreme Matter Observatory kilohertz-band gravitational wave detector design concept.

DOI: 10.1103/PhysRevD.102.122003

I. INTRODUCTION

The next generations of gravitational wave (GW) detectors call for extremely high circulating optical power to reduce the impact of quantum noise at frequencies beyond a few hundred Hertz up to several kilohertz. Improved sensitivity in this frequency band is critical for studying fundamental nuclear physics with constraints on the equation of state (EOS) of neutron star matter. Postinspiral waveforms of binary neutron star (BNS) mergers, which can contain the ringdown signatures of nascent hypermassive neutron stars or black holes, are particularly useful to inform the EOS in the hot regime [1]. Significant sensitivity enhancements in the kilohertz-band are required to achieve this, since virtually all models feature relevant frequency content above 1 kHz.

Additional information can be obtained by measuring deformations of neutron stars from spherical shape. This can be achieved with the yet-to-be-observed gravitational wave emission from spinning neutron stars, which is likely to occur in the kilohertz frequency regime [2]. Further significant advances in nuclear physics will be possible if the cold equation of state is measured by accurately detecting the tidal disruption of BNS systems at the end of their inspiral [3,4].

A general concept for a dedicated detector that targets the low kilohertz frequency range, named Neutron Star Extreme Matter Observatory (NEMO), has evolved out of the OzHF design study for a next-generation instrument in Australia. The proposed sensitivity of NEMO is comparable to third-generation detectors above 1 kHz at a fraction of the cost and could be achieved substantially sooner. The addition of NEMO to a network of two Advanced LIGO (aLIGO) detectors at the A+ sensitivity level could increase the expected event rates for the detection of postmerger remnants from approximately one in several decades to a few per year. NEMO may also allow the first GW observations of signals from isolated neutron stars and other exotica. Any of these observations will greatly expand our knowledge of nuclear physics under a large range of conditions that are not accessible on the laboratory scale on Earth. The complete science case and its implications are discussed in detail in Ref. [5]. In this paper, we concentrate on a specific technical aspect of building NEMO: how to achieve thermal equilibrium at high optical power with minimal design complexity.

*johannes.eichholz@anu.edu.au

Several megawatts are required to circulate in the arm cavities to gain access to the BNS merger signature in the waveform [6]. In addition, to achieve peak sensitivity near 2 kHz, an optical power on the order of 30 kW is needed to be incident on the beam splitter (BS) [7]. At such power levels, optical absorption in substrates and coatings induces strong thermal aberration effects in the fused silica test masses of contemporary GW detectors [8–11]. In particular, the thermal distortion caused by absorptive point defects in the high reflection (HR) test mass coatings introduces higher-order spatial deformations of the mirror surface. This perturbs the wave fronts and results in severe power-dependent scatter loss which can limit the power build up in the arm cavities [12].

Crystalline silicon has far higher thermal conductivity than amorphous silica and is better suited as a substrate material to suppress the formation of steep temperature gradients. Further, the thermal conductivity of silicon increases as its temperature reduces. In addition, the coefficient of thermal expansion (CTE) of crystalline silicon crosses zero at 123 and 18 K. Unfortunately, silicon's thermo-optic coefficient is higher than that of silica. In combination, these factors grant silicon test masses a massive reduction in mirror thermal surface distortion and a less pronounced but still significant reduction in thermal lensing when operated in the vicinity of 123 K.

Cryogenic operation using radiative cooling of the test masses is conceptually simpler than resorting to conductive cooling through suspension wires. But the efficiency of radiative cooling reduces rapidly as temperature decreases, owing to the T^4 dependence of thermal emission. At 123 K, several watts of heat extraction can be achieved, making a radiative-only approach feasible for the LIGO Voyager [13] proposal. Operation below 18 K is likely only possible with conductive cooling and limited optical power, which is proposed for the low frequency part of Einstein Telescope [14] and currently being pioneered by the sapphire-based KAGRA detector [15]. The NEMO baseline requires in excess of 10 W to be extracted from the test masses to achieve kilohertz strain sensitivity at the 10^{-24} $\mathrm{Hz}^{-1/2}$ level.

A radiatively cooled dedicated kilohertz-band detector can be designed with significant simplifications compared to broadband detectors due to relaxed tolerances for low frequency thermal and environmental noises. In particular, triple-stage metal wire test mass suspensions and minimal seismic preisolation are sufficient to suppress seismic noise. These are much simpler than the complex systems used in aLIGO [16,17] or Virgo's superattenuator [18,19], both of which feature a final monolithic silica suspension stage to reduce suspension thermal noise. A simpler system reduces both the cost and complexity of installation and commissioning tasks. In this paper, we show that quantum noise limited operation can be achieved in an NEMO detector using three-stage steel wire and spring blade suspensions.

The paper layout is as follows: we first describe the configuration of the detector, followed by a discussion of its suspensions and thermal equilibrium in the system. We then explore an increase of the test mass temperatures to equalize the thermal budget and the effect it has on thermal lensing and thermal noise. Based on these considerations, we present a conceptual noise budget for the elevated temperature scenario. Last, we discuss the applicability of our proposed approach for broadband GW detectors.

II. DETECTOR CONFIGURATION

The full justification for the NEMO interferometer design is presented in Ref. [5]. Here we provide only a brief description of the detector, which is based on the LIGO Voyager proposal by Adhikari *et al.* [13]. The proposed layout, which is illustrated in Fig. 1, is based on the cavity-enhanced, dual-recycled Michelson configuration of aLIGO [20], Advanced Virgo [21], and KAGRA [15], with an arm length of 4 km. Table I provides a parameter summary. NEMO uses cryogenically cooled silicon test masses for improved power handling and reduced thermal noise. A carrier wavelength around

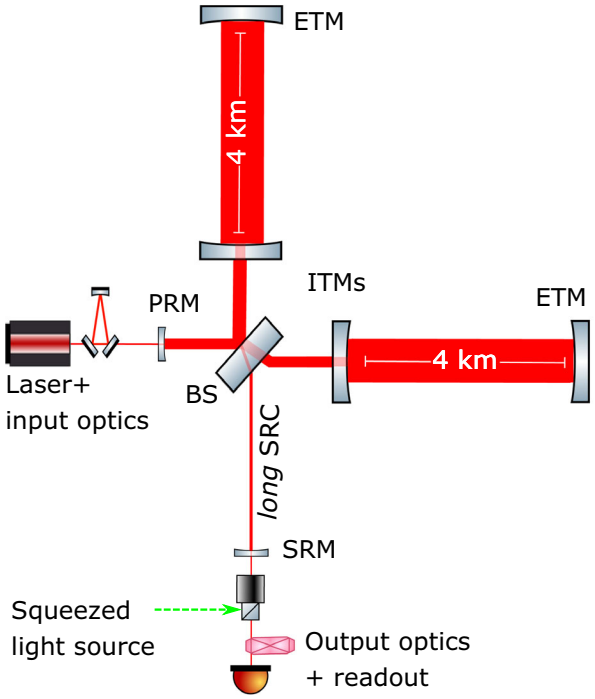

FIG. 1. Simplified optical layout of the NEMO detector concept. The primary optics are the input and end test masses (ITM and ETM, respectively) that form the arm cavities, the BS, the power recycling mirror (PRM) that maximizes power buildup in the interferometer, and the signal recycling mirror (SRM). The signal recycling cavity (SRC) shapes the detector response, and with 354 m it is significantly longer than the SRCs currently featured by LIGO and Virgo. Squeezed vacuum is injected through the output port to suppress quantum noise.

2 μm is chosen because 1.064 μm used in silica and sapphire-based interferometers is absorbed by silicon.

The NEMO substrates consist of high-purity single-crystal silicon grown by the magnetic Czochralski (mCz) method [22] and have a diameter of 45 cm. The thickness is set to 20 cm, identical to aLIGO but significantly thinner than the 55 cm planned for LIGO Voyager. The resulting mirror mass is 74.1 kg.

The NEMO design assumes an input laser power of 500 W, which results in 4.5 MW circulating in the arms. About 10 dB of broadband phase-squeezed vacuum is injected into the detector through the dark port which reduces the quantum noise by 7 dB after accounting for optical losses. The crossover between quantum radiation pressure noise (QRPN) and quantum shot noise for NEMO occurs at about 42 Hz. This marks the frequency at which squeezed states would need to be rotated by means of a filter cavity or photon entanglement [23–25] to simultaneously reduce both quantum noises. Since NEMO is focused at high frequencies only, no frequency-dependent rotation of squeezed states is necessary to suppress QRPN. NEMO uses the long signal recycling cavity (SRC) approach of Miao *et al.* [7,26–28] which reduces sensitivity to optical losses in the SRC. NEMO sets itself apart from other detector proposals in that it aims exclusively for kilohertz sensitivity and makes no demands below 500 Hz. This presents several opportunities to simplify detector subsystems and favor established technologies over increased detector complexity.

The power recycling mirror (PRM) transmission is set to 3%, which maximizes the power buildup in the interferometer. The corresponding power recycling gain is 63, which amounts to 31 kW in the power recycling cavity (PRC), and 4.5 MW in the arm cavities. A 354 m long SRC with a signal recycling mirror (SRM) transmission of 4.8% results in a coupled cavity system that resonantly enhances GW signals in the range 1 to 3 kHz.

The radii of curvature of the test masses have been chosen to provide large beam sizes for low thermal noise and suitable frequency spacing of higher-order cavity modes. However, the combination of high intracavity power and test mass dimensions warrants an investigation of potential parametric instabilities [29]. These instabilities arise due to test mass mechanical modes that scatter Doppler-shifted carrier light into higher-order transverse modes of the suspended optical cavities. An oscillating radiation pressure force due the beat between these higher-order modes and the carrier light then further excites the test mass mechanical modes, leading to a run-away effect. An in-depth analysis of this issue is currently underway [30].

The optical absorption in mCz silicon—generally a combination of different absorption processes and also subject to change with temperature—is not yet fully understood. Like in Voyager, interband absorption is expected to play a negligible role [13]. Based on measurements reported in Ref. [31], we calculate sub-ppm levels of two-photon absorption in NEMO. The theoretical free-carrier absorption due to residual doping at typical resistivity levels of high-purity silicon (several thousand Ωcm), which roughly correspond to carrier concentrations of 10^{12} to 10^{13} cm^{-3}, is only about 1 ppm/cm [13].

An optical absorption of 4.3 ppm/cm has been reported at 1550 nm for 10 kΩcm n-type float-zone silicon, the majority of which was attributed to an absorption band at 2.3 μm [32]. The dominant impurities in mCz silicon are sites of interstitial oxygen, which can turn into thermal charge carrier donors during annealing [13] that increase absorption. To date, mCz silicon has shown the potential for excellent absorption; however, significant inhomogeneity has also been observed and it is not yet clear that a large enough piece with sufficiently low absorption can be obtained with this growth method. Further research is required to mitigate absorption and improve homogeneity. For the NEMO case, we assume an optical absorption of 10 ppm per cm at 2 μm, independent of temperature.

The resulting round-trip absorption loss in each NEMO test mass is 400 ppm. Compared to this number, scatter loss due to impurities in the substrates is negligible [13]. A summary of optical losses in the test masses and recycling cavities is listed in Table I. The absorption, thermal lensing, and scatter loss of the BS, which is budgeted at 150 ppm, depends on the choice of material, size, and thickness, and is an ongoing research issue and not further discussed here.

The current generation of detectors uses coatings made of alternating layers of silica (SiO_2) and tantala (Ta_2O_5) doped with titania (TiO_2) [33]. These coatings have excellent optical properties in the 1–2 μm range. Their Brownian noise is predominantly caused by the high mechanical dissipation in the tantala layers. The loss angle of the titania/tantala alloy is 3.6×10^{-4} at 100 Hz at room temperature with a weak frequency dependence [34], while that of silica is 4×10^{-5} [35]. Coating Brownian noise approximately scales with the square root of the overall coating thickness as well as the square root of the compound coating loss angle, which is an average of the individual material loss angles weighted by their contribution to the total coating thickness. It is therefore desirable to minimize the physical coating thickness in addition to using low-loss materials. Using the well-studied tantala/silica coatings in an NEMO detector would result in a small thermal noise penalty in the kilohertz regime compared to novel low noise coatings. In our design study, we considered two other coating species: amorphous silicon/silica coatings and crystalline GaAs/AlGaAs coatings. In the text below, we refer to these as a-Si and AlGaAs coatings, respectively.

a-Si has low mechanical loss of about 10^{-5} at cryogenic temperatures [36] and a very high index of refraction of 3.5 [37]. When paired with silica, the large refractive index

TABLE I. NEMO optical parameters used in the calculation of the noise traces featured in Fig. 2. The round-trip loss contributions of input test masses (ITMs), BS, and SRM are listed separately, and the total SRC loss is calculated as the sum of all losses in both arms.

Parameter	Value
Input power	500 W
Laser wavelength	2 μm
Arm length	4 km
SRC length	354 m
ITM and ETM mass	74.1 kg
ITM curvature	1800 m
ETM curvature	2500 m
ITM beam radius	58.8 mm
ETM beam radius	83.9 mm
ITM transmission	1.4%
ETM transmission	5 ppm
PRM transmission	3.0%
SRM rantsmission	4.8%
Arm cavity loss	40 ppm
ITM substrate absorption	400 ppm
ITM residual thermal lensing and scatter	160 ppm
SRM optical loss	150 ppm
BS optical loss	150 ppm
Total SRC loss	1500 ppm
Reduction in quantum noise	7 dB

contrast of the two materials dramatically reduces the number of coating layers and overall coating thickness. The mechanical loss of silica increases as temperature reduces below room temperature [38,39], but at 123 K this effect is still moderate, which allows LIGO Voyager to consider a-Si/SiO_2-coatings. A potential issue of these coatings is an uncertain optical absorption of a-Si. An estimate of 20 ppm was made for a 2 μm HR coating stack based on measurements performed at 47 K [40]. Further, an a-Si coating with a 7.6 ppm absorption was demonstrated at 1.55 μm [41], and an extrapolation suggesting a-Si coatings may have sub-ppm absorption at 123 K and 2 μm was made in Ref. [13].

Crystalline AlGaAs coatings offer low mechanical loss on the order of 2×10^{-5} and low optical scatter and absorption have been demonstrated [42,43]. Both GaAs and AlGaAs have high refractive indices at 2 μm of 3.3 and 2.9, respectively, making individual layers very thin. However, the small refractive index contrast requires a significant number of layers to form an HR coating. For example, at least 93 individual layers with a total thickness exceeding 15 μm are required to achieve the desired 5 ppm end test mass (ETM) transmission. AlGaAs coatings are also not lattice matched to silicon and have to be grown on separate GaAs wafers. Epitaxial growth and substrate transfer have been demonstrated for 80 mm diameter coatings with encouraging results [44], but available GaAs wafer size and transfer technique scaling present challenges for the application of large area AlGaAs coatings.

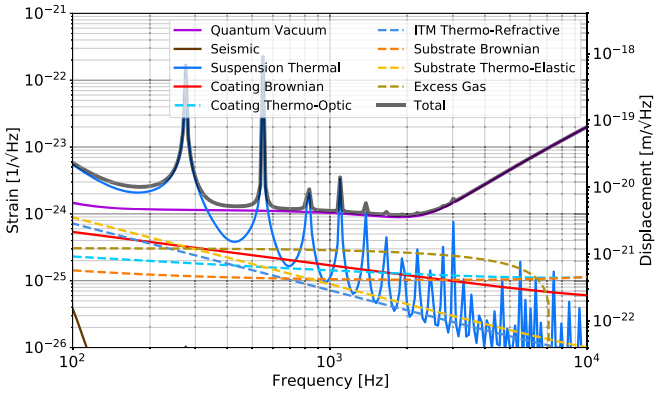

FIG. 2. Conceptual noise budget of an NEMO detector. With the exception of a small number of violin modes in the final stage of the triple suspension, the detector is quantum noise limited above 500 Hz.

Both a-Si and AlGaAs coatings are optically suited for the 2 μm wavelength. Additional research will likely reduce the absorption seen in a-Si coatings. However, their fundamental absorption limit, which is a critical issue for NEMO because of its high circulating power, remains uncertain at this point. For this reason, we consider crystalline AlGaAs coatings in this work, with an assumed coating absorption of 1 ppm. We do note, however, that scaling AlGaAs coating sizes up by the required factor of 5 is a costly and potentially time consuming process. If a 1 ppm absorption can be confirmed in a-Si coatings, they would present a similarly, if not more viable coating solution with negligible thermal noise impact on the NEMO detector.

Figure 2 shows a noise budget that includes quantum, thermal, and environmental noise traces, along with their incoherent sum. Above 1 kHz the detector is principally quantum-noise limited. This noise budget is contingent on several discussion points around which this paper revolves and which need to be justified in detail: suspension design and materials, test mass operating temperature, and thermal noise.

III. SUSPENSIONS

Gravitational wave interferometers utilize suspensions to isolate their test masses from ground motion and to provide a low noise actuation platform. The type of the suspension system determines the complexity of the associated control scheme, and adds additional noise sources—principally suspension thermal noise [45]. Kilohertz instruments like NEMO have relaxed requirements on seismic isolation and suspension thermal noise, because these noises sources are not dominant at kHz frequencies.

A conceptual triple stage suspension design, similar to those used for the auxiliary optics in Advanced LIGO [46],

TABLE II. NEMO suspension parameters. All three stages use ASTM A229 steel musical wires. The upper two stages use spring blades made from Maraging 250 Steel for vertical isolation. No spring blades are used in the final stage.

Stage	Final	Penultimate	Top
Suspended mass (kg)	74.1	37.0	37.0
Number of wires	4	4	2
Wire length (mm)	550	450	350
Wire diameter (μm)	550	700	1100
Blade deflection (mm)	⋯	5.0	10.0
Blade thickness (mm)	⋯	4.59	5.05
Blade spring constant (N/mm)	⋯	54.5	72.6

is assumed for NEMO. Each stage consists of steel wires which attach to the previous stage and support a reaction mass, or the test mass in case of the lowest stage. Blade springs [47] are used in the first two stages to provide vertical isolation. The bottom stage is radiatively cooled, with both upper stages remaining at room temperature. The dynamic parameters for each stage are given in Table II.

Violin modes of the final stage are the only notable source of suspension thermal noise that affects the NEMO sensitivity in the kilohertz-band. Their frequencies are primarily effected by the length, linear mass density, and tension of the suspension wires [48]. The Q-factors are determined by their bending profiles and the intrinsic material loss, surface losses, and thermoelastic loss, particularly in regions where the deformations are largest. These modes are generally narrow in frequency but can saturate the detector output and need to be damped. It is desirable to minimize their number in the detection band.

For the NEMO detector, we assume the use of ASTM A229 piano wire, which has high yield stress up to 3 GPa and low creep under stress. This allows very thin suspension wires to be used, which increases the frequency spacing of the violin modes as well as gravitational dilution [49]. As most of the energy in a pendulum system is stored in the dissipation-less local gravitational field, the pendulum mechanical loss can be orders of magnitude lower than the intrinsic material loss of the wires. This benefits the associated suspension thermal noise, offsetting the higher mechanical and thermoelastic loss of steel compared to silica or cryogenic silicon ribbon suspensions. The small mass and inertia of the steel wires are beneficial for reduced coupling of violin modes to test mass displacement [45,50]. Metal wire suspensions are a simple, mature technology that should reduce the commissioning time.

A state space system for three coupled oscillators is used to derive the suspension thermal and seismic noise for the longitudinal and vertical degrees of freedom. The spring constants are calculated by adopting the methodology outlined in Refs. [48,51], which derive the violin modes from the Euler-Bernoulli beam equation. Cross-coupling between and from other degrees of freedom is neglected at this conceptual stage.

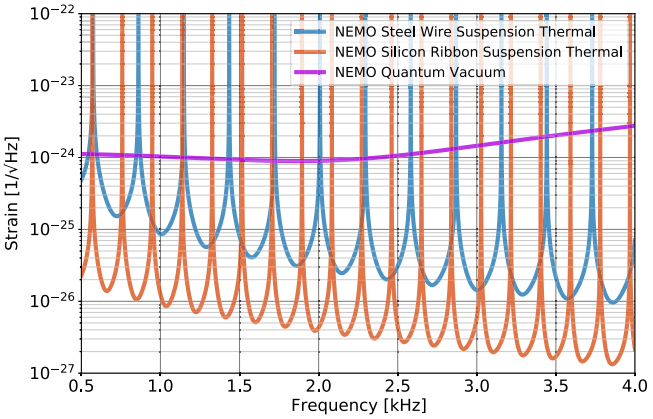

FIG. 3. Comparison of the suspension thermal noise in silicon ribbon suspensions and steel wire suspensions. The peaks correspond to analytically calculated violin mode frequencies of the ribbons or wires. The quantum noise, the only other dominant noise in this frequency interval, is also shown. Due to the lower yield strength in silicon ribbons, the frequency spacing is smaller, resulting in a larger number of modes in the NEMO sensitivity band.

For comparison, we also consider a final stage using silicon ribbons similar to the LIGO Voyager design. While silicon has large intrinsic tensile strength, thin ribbon suspensions are currently limited to a yield strength $\mathcal{O}(100$ MPa) [52]. Figure 3 shows the suspension thermal noise traces for both cases. For the calculation, a stress of 100 MPa was considered in the rectangular silicon ribbons with an aspect ratio of 10, and 760 MPa in the round steel wires.

In the NEMO configuration, the dominant loss of the silicon suspensions originates in the thermoelastic loss at the warm top of the final stage. In detectors with cryogenic penultimate stages, this effect is suppressed. The silicon thermal noise has a lower baseline level, but smaller mode spacing and therefore more peaks in the detection band. More resonances with higher Qs require better damping and can result in substantial lost time during lock acquisition. On the other hand, the steel wire resonances occupy a broader cumulative frequency range in which suspension thermal noise exceeds the quantum noise baseline. We calculate a lost bandwidth of 61 Hz for steel suspensions between 1 and 3 kHz, while that of silicon ribbons is only 7 Hz. This comparison does not consider mode degeneracy or cross-coupling between modes, which could become an issue particularly in the flat silicon ribbons and introduce more mode frequencies to be considered. It should be mentioned that with sufficiently accurate modal monitoring of the suspension wires, coherent subtraction of the associated suspension noise from the GW data stream may be possible. We conclude that the NEMO concept, which does not rely on thermal conduction

and has a warm penultimate stage, is better aligned with steel suspensions.

IV. THERMAL BUDGET

At 123 K, a black body of the proposed NEMO test mass shape emits a total of 7.8 W of thermal radiation. A detailed study using finite element simulations for LIGO Voyager has shown that a radiative cooling rate of 70% of the equivalent black-body radiation of its larger test masses can be achieved [13]. We assume the same cooling efficiency for NEMO, which accounts for subunity surface emissivities, incomplete cryogenic shroud coverage, and finite shroud temperature. This reduces the radiative cooling rate to 5.5 W at 123 K.

A 1 ppm coating absorption of the circulating 4.5 MW generates a heat load of 4.5 W on the test masses. Thermal conduction through the four steel suspension wires from a 295 K penultimate stage to a 123 K test mass is small by comparison, contributing only an additional 10 mW. The HR surfaces of the ETMs ensure that the beams transmitted through the ETMs are low in power and add only 4.5 mW of bulk heating. On the other hand, significant power (15.5 kW) is transmitted through the input test mass (ITM) substrates because they are part of the PRC. This makes substrate absorption significant and adds 6.2 W of substrate heating for a total of 10.7 W absorbed in each ITM.

The barrel surface is generally more efficient at cooling per unit area since it can be endowed with high emissivity coatings and sees more complete cryogenic shroud coverage than the test mass faces. The high circulating power in the PRC, paired with the high absorption in silicon, results in more power absorbed per unit length than cooling power gained per unit length from increasing the test mass thickness. Hence, thinner ITMs are favorable both from a thermal perspective and to minimize recycling cavity losses.

The heat load absorbed in the ITMs is nearly twice the radiative cooling rate at 123 K, which means their temperature cannot be sustained during high power operation. The quartic temperature dependence of radiative heat transfer implies that even a small increase of the test mass temperature can add significant radiative cooling power. Assuming the above efficiency of 70% of the equivalent black body radiation, the cooling rate increases to 6.8 W at 130 K, to 9.2 W at 140 K, and 12.1 W at 150 K. This is sufficient to compensate the combined coating, substrate, and suspension heating effects in the ITMs. For the NEMO design, we therefore assume an ITM temperature of 150 K, whereas there is no need to raise the ETM temperature, which remains at 123 K.

It should be noted that the effective emissivities of the test mass surfaces at thermal wavelengths ranging from 10 to 30 μm are not confirmed. Both AlGaAs coatings and silicon have penetration depths on the order of the test mass dimensions or longer in the mid-IR. The test mass barrel can be coated with a high emissivity coating, but the surface area of the NEMO test masses is dominated by their end faces, where this is not possible. However, the antireflective test mass coatings facing away from the arm cavities are likely to use silica layers, which are opaque at thermal wavelengths and therefore likely to enhance emissivity. If the AlGaAs HR coatings are found to severely compromise the radiative cooling rate, a-Si and tantala-silica coatings represent fallback options, as both contain silica layers and have tolerable thermal noise, which is discussed in Sec. VII.

V. WAVEFRONT ABERRATIONS

Straying from the CTE null of crystalline silicon increases the impact of thermal distortion and elevating the temperature increases thermal lensing. This is because increasing the temperature reduces the thermal conductivity and increases both the thermo-optic and thermoexpansion coefficients. These aberrations are primarily created due to the radial temperature gradients formed in the test mass.

To quantify the thermal aberration performance as a function of temperature, we define two figures of merit, FOM_α and FOM_β, as

$$\mathrm{FOM}_\alpha(T) = \frac{\kappa_{\mathrm{Si}}(T)}{\kappa_{\mathrm{SiO_2}}(300\ K)} \times \frac{\alpha_{\mathrm{SiO_2}}(300\ K)}{\alpha_{\mathrm{Si}}(T)} \tag{1}$$

for the geometric distortion, and

$$\mathrm{FOM}_\beta(T) = \frac{\kappa_{\mathrm{Si}}(T)}{\kappa_{\mathrm{SiO_2}}(300\ K)} \times \frac{\beta_{\mathrm{SiO_2}}(300\ K)}{\beta_{\mathrm{Si}}(T)} \tag{2}$$

for the refractive distortion of the test masses, where κ, α, and β are the thermal conductivity, the coefficient of thermal expansion, and the thermo-optic coefficient of the indexed material, respectively. These figures of merit are defined inversely to those introduced for a similar discussion in Ref. [53] and normalized to silica at room temperature, such that their magnitude directly represents a performance improvement factor. These figures of merit compare the thermal aberration sensitivity of cryogenic silicon to that of room temperature silica.

In Fig. 4, we plot both as functions of temperature using the material properties illustrated in Fig. 5 and note the singularity of FOM_α at 123 K. At the proposed ITM temperature of 150 K, FOM_α has value of roughly 300. Geometric distortions are suppressed by this factor compared to room temperature fused silica, assuming the absorbed powers are equal. The difference in FOM_β reduces less dramatically from 60 at 123 K to 33 at 150 K, which is still a large improvement over fused silica at room temperature.

A large issue of current GW detectors that hinders an increase in circulating power are absorptive point defects in the HR coatings of the test masses. Their random

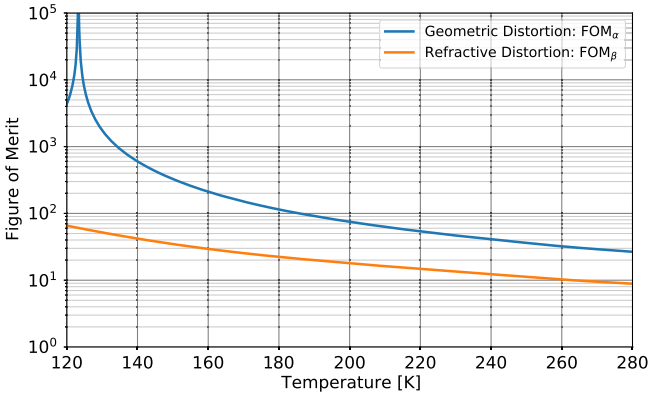

FIG. 4. Thermal distortion figures of merit FOM$_\alpha$ and FOM$_\beta$ for silicon vs silica as functions of temperature. The large thermal conductivity of silicon enhances both significantly above unity. FOM$_\alpha$ also profits from the vanishing thermal expansion, which becomes most apparent in the singularity at 123 K.

distribution, combined with the low thermal conductivity of fused silica, can create higher-order spatial aberrations of the reflecting surfaces that are difficult to correct with thermal compensation systems. The result is a scatter loss that increases with optical power. This purely geometric effect is significantly suppressed in a silicon-based detector. In its first observation run, aLIGO had already reached an arm cavity power of 100 kW [54]—far more than the proposed 4.5 MW divided by the relief factor of 300 of a 150 K ITM. The problem of point absorbers only appeared after roughly doubling this power. We can conclude that ITM deformations due to uniform HR coating absorption and a comparable number of point absorbers present a far smaller issue to an NEMO detector and are not prohibitive of the proposed power levels.

There are two more thermal distortion effects in the ITMs that deserve attention. The first is the deformation of the ITM HR coated surface due to power absorbed in the substrate. This is again a geometric effect, suppressed by FOM$_\alpha$, but the absorbed power is higher. Fused silica absorbs on the order of 0.5 ppm/cm at 1.064 μm, which is a factor of 20 smaller than the assumed absorption in mCz-silicon at 2 μm. Additionally, the power in the power recycling cavity is a factor of 5 higher than in aLIGO at design sensitivity. Since the test masses have the same thickness, NEMO ITMs absorb 100 times more power. Fortunately, the FOM$_\alpha$ value of 300 is still large enough to push the combination of all factors below unity, indicating that the ITM HR surface deformation due to substrate absorption in an NEMO detector is less significant than in current observatories.

The second, more detrimental effect is thermal lensing in the ITM. The reason is that the suppression of temperature gradients by the high thermal conductivity of silicon is partially counteracted by its higher thermo-optic coefficient, which is reflected in the significantly smaller values of FOM$_\beta$ compared to FOM$_\alpha$. In combination with the higher absorbed power, thermal lensing becomes more pronounced than in aLIGO. We estimate the scatter loss in

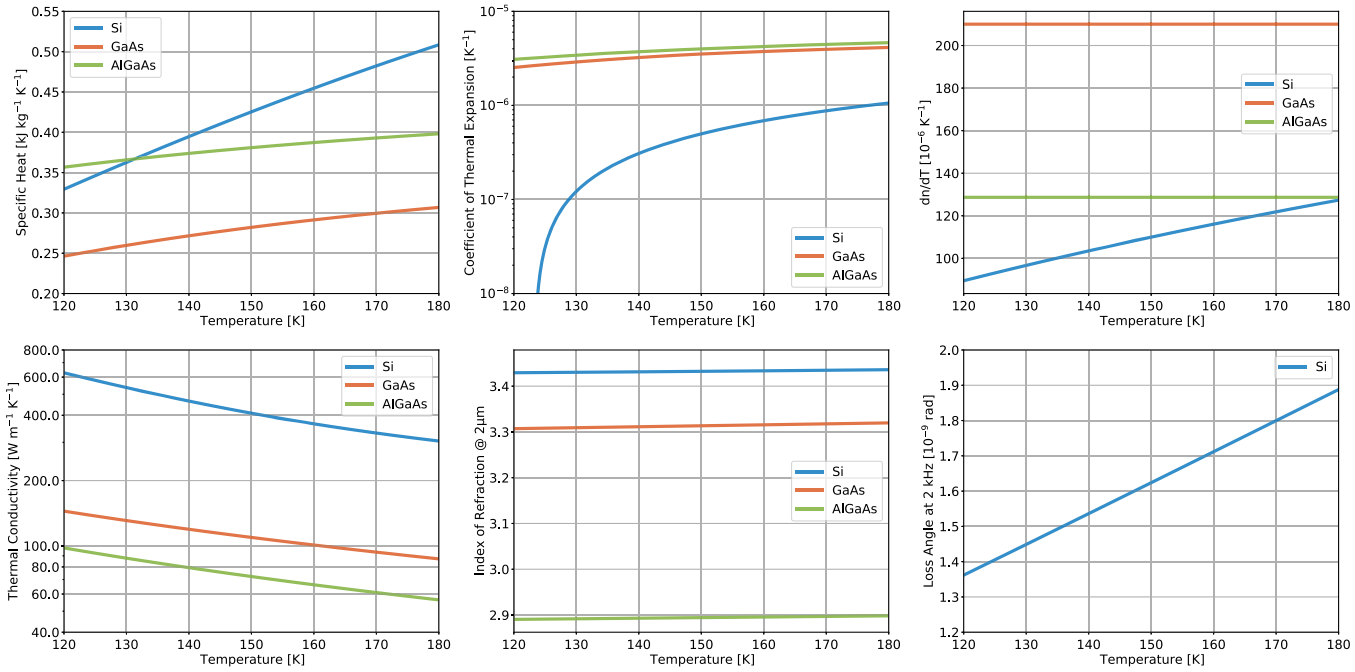

FIG. 5. Temperature dependencies of select material parameters used in the calculation of thermal noise. The bottom right plot shows only the bulk mechanical loss of silicon, which has a $1/f$ frequency dependence and was evaluated at the NEMO peak sensitivity frequency 2 kHz. No temperature or frequency dependence is assumed for the thin-film loss angles of GaAs and AlGaAs, which are both estimated at 20 μrad and have been omitted from this figure.

the ITM substrates $S(T)$ due to thermal lensing from the absorbed power P_{abs} for the wavelength λ with the expression

$$S(T) = 40\ \mathrm{ppm}\left(\frac{1.4\ \mathrm{Wm^{-1}\,K^{-1}}}{\kappa_{\mathrm{Si}}(T)}\right)^2 \times \left(\frac{\beta_{\mathrm{Si}}(T)}{10\ \mathrm{ppm/K}}\right)^2\left(\frac{1\ \mu\mathrm{m}}{\lambda}\right)^2\left(\frac{P_{\mathrm{abs}}}{1\ \mathrm{mW}}\right)^2, \quad (3)$$

which was taken from Ref. [11] and applies to a double pass through the ITM. As can be seen, the transition to 2 μm has a beneficial impact in this expression. Assuming a theoretically possible suppression of 10^4, which is also derived in Ref. [11], the optical loss due to thermal lensing per round-trip through the ITM becomes 160 ppm, which was included in the modeling of the recycling cavities.

The suppression level required presents a serious challenge for the thermal compensation system in NEMO. Inhomogeneity in the absorption profile would make this task even more difficult. Any small improvement to substrate absorption would have enormous benefits for thermal lensing due to a combination of factors. The corresponding reduction in absorbed power, which appears squared in Eq. (3), would allow the ITM temperature to decrease, which in turn increases κ_{Si} and reduces β_{Si}.

VI. THERMAL NOISE AT ELEVATED TEST MASS TEMPERATURE

We identify six sources of thermal noise to be of importance to an NEMO detector and investigate their temperature dependence. Five of these directly modulate the optical path length of the arm cavities, namely, substrate Brownian and thermoelastic noise [55,56], coating Brownian and thermo-optic [57–61], and suspension thermal noise [48,62]. The remaining noise source, ITM thermorefractive noise [63], enters the differential readout of the Michelson topology, but is suppressed by the finesse of the arm cavities. Theoretical studies of carrier density noise in the ITMs and BS suggest that it will be a negligible source of differential length noise [63,64].

The amplitude of Brownian noise in coatings, substrates, and suspensions has an explicit $\sqrt{T}$ dependence [45,55]. Thermoelastic and thermorefractive noises have a stronger explicit temperature dependence $\propto T$, and the temperature dependence of material parameters also folds into the detailed thermal noise models. The characteristics associated with thermoelastic and thermo-optic noise, namely, the CTE α_i, thermorefractive coefficient β_i, thermal conductivity κ_i, and specific heat capacity C_i, tend to have a stronger temperature dependence than the mechanical properties Young's modulus Y_i, Poisson's ratio σ_i, and mechanical loss ϕ_i that appear in models for Brownian noise. In particular, the thermoelastic noise of silicon substrates deserves attention, as the thermal expansion of silicon undergoes the most notable change.

Figure 5 shows the temperature dependence of select material properties of crystalline silicon, GaAs, and AlGaAs that were used in the thermal noise calculations. Data for C_{Si} were taken from Ref. [65] and for κ_{Si} from Ref. [66], which report typical thermal conductivity values for high-purity Si. This choice was made since GW detector test masses require high purity and negligible doping levels to avoid free carrier absorption. In the relevant temperature range, this κ_{Si} is consistent with that of Ref. [67] for oxygen-free, residually p-doped silicon with a carrier density of order 10^{13} cm^{-3}, which is the expected level for the NEMO mCz test masses. The silicon CTE α_{Si} was calculated based on Ref. [68]. The index of refraction n_{Si} and β_{Si} was derived from data presented in Ref. [69].

Omitted from Fig. 5 due to their weak temperature dependence are the densities, Young's moduli, and Poisson's ratios. For the thermal noise calculations, ρ_{Si} was taken from Ref. [68], Y_{Si} and σ_{Si} were derived from the elastic constants presented in Ref. [70], and ϕ_{Si} was calculated based on the principle relaxation process identified in Ref. [71]. The densities ρ_i, Young's moduli Y_i, and Poisson's ratios σ_i of silicon, GaAs, and AlGaAs show only little variation between 100 and 300 K of less than 1%. The mechanical loss angle ϕ_{Si} of silicon is 17% higher at 150 K than at 123 K and roughly double at room temperature. The loss angle ϕ_i in GaAs and AlGaAs is less well known as a function of temperature in the shown range and assumed as 2×10^{-5} independent of temperature [72].

The properties of the AlGaAs coatings that are also shown in Fig. 5 are less well documented in the literature. Some can be calculated based on crystal structure and molecular properties, but to do so was outside the scope of this study. Instead, we used GaAs and AlAs material parameters and their temperature dependence as available, used linear interpolation when only known for select temperatures, and otherwise assumed their room temperature values. Select $\mathrm{Al}_x\mathrm{Ga}_{1-x}\mathrm{As}$ properties for the AlAs content x were calculated via interpolation between GaAs and AlAs as

$$X_{\mathrm{Al}_x\mathrm{Ga}_{1-x}\mathrm{As}}(T) = xX_{\mathrm{AlAs}}(T) + (1-x)X_{\mathrm{GaAs}}(T). \quad (4)$$

This formula was used to interpolate the nontransport properties density, Young's modulus, Poisson's ratio, specific heat capacity, and coefficient of thermal expansion. Following published results for thermal noise in AlGaAs coatings, we work under the assumption $x = 0.92$ [73]. The plots for κ_{GaAs}, κ_{AlGaAs}, C_{GaAs}, and C_{AlGaAs} in Fig. 5 were obtained and partially extrapolated from data in Refs. [74,75], whereas α_{GaAs} and α_{AlGaAs} were taken from Refs. [76,77]. The indices of refraction of GaAs and AlGaAs were interpolated between known values at 123 and 300 K [72], and the thermo-optic coefficients were assumed constant for consistency.

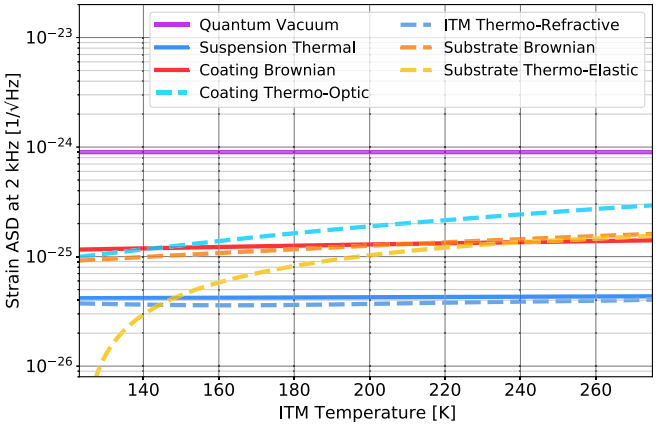

FIG. 6. Noise amplitude of an NEMO detector at 2 kHz in units of astrophysical strain and as a function of ITM temperature. The ETM temperature was held constant at 123 K for the shown noise traces.

The calculation of coating thermal noise requires knowledge of the coating thickness and layer structure for the HR coating. To this end, we assume a quarter-wave design with transmission tuning via the thickness of the lowest layer and obtain an estimate of the total coating thickness. This leads to a coating thickness of 15.2 μm on the ETM and 5.8 μm on the ITM, respectively. In reality, the coating topology will be subject the transmission requirements at other wavelengths used for control during lock acquisition. It can also be optimized to minimize thermo-optic noise by taking advantage of partial coherence between thermorefractive and thermoelastic noise [60,73]. The lower temperature of the ETM in NEMO partially compensates the higher thermal noise generation due to its thicker coating.

We use the GWINC software package [78] to calculate the levels of the different thermal noises at 2 kHz as functions of temperature, subject to the above coating topology and material parameters. The result is plotted in Fig. 6 against the baseline quantum noise level at that frequency. This process required small modifications to the GWINC code base to allow different ITM and ETM temperatures.

At the current stage, GWINC's built-in method for calculating coating Brownian noise does not distinguish losses for bulk and shear deformations. Instead, the two are assumed to be comparable and a single representative loss value is used. Detailed models have shown that losses for bulk and shear deformations have to be treated separately [59]. For AlGaAs, a crystalline material with built-in anisotropy, this can become particularly relevant. Both types of loss parameters are accessible via mechanical oscillator ringdown time constant measurements [79], and it has been shown that this assumption may not hold for AlGaAs [44].

All primary sources of thermal noise are within close proximity of each other, but have a significant margin of nearly an order of magnitude to the NEMO detector's quantum noise level below 160 K. The plot clearly shows the stronger temperature dependence of thermo-optic and thermoelastic noise, while ITM thermorefractive and suspension thermal noises are nearly independent of temperature. It is clear that the thermal noise of silicon test masses and AlGaAs coatings does not become a limiting performance factor for an NEMO detector even for temperatures higher than 150 K.

VII. DISCUSSION

We now have the complete information to fully assemble the NEMO detector noise budget that was presented in Fig. 2. Table III explicitly lists those material properties of

TABLE III. Substrate, coating, and suspension material properties at 123 and 150 K used in the calculation of thermal noise in the NEMO detector.

Parameter	Material	123 K	150 K
Young's modulus (GPa)	Si	131.1	131.0
	GaAs	87.61	87.35
	AlGaAs	83.83	83.81
	A229 Steel	212.0	212.0
Poisson's ratio	Si	0.279	0.279
	GaAs	0.312	0.312
	AlGaAs	0.323	0.323
Mechanical loss (10^{-6} rad)	Si[a]	0.00139	0.00162
	GaAs	20.0	20.0
	AlGaAs	20.0	20.0
	A229 Steel	190.0	190.0
Specific heat ($\mathrm{J\,kg^{-1}\,K^{-1}}$)	Si	339.4	425.4
	GaAs	250.5	282.0
	AlGaAs	359.5	380.9
	A229 Steel	250.0	287.0
Thermal conductivity ($\mathrm{W\,m^{-1}\,K^{-1}}$)	Si	598.3	409.0
	GaAs	140.2	109.4
	AlGaAs	94.6	72.2
	A229 Steel	15.0	20.3
Coefficient of thermal expansion (10^{-6} $\mathrm{K^{-1}}$)	Si[b]	0.001	0.498
	GaAs	2.642	3.519
	AlGaAs	3.183	3.988
	A229 Steel	8.0	8.6
Thermo-optic coefficient (10^{-6} $\mathrm{K^{-1}}$)	Si	91.7	110.0
	GaAs[c]	210.0	210.0
	AlGaAs[c]	128.7	128.7
Refractive index	Si	3.430	3.432
	GaAs[c]	3.308	3.313
	AlGaAs[c]	2.891	2.894

[a]The bulk mechanical loss of silicon follows a power law $\propto f^{-1}$: the listed loss was evaluated at 2 kHz.
[b]The thermal expansion of silicon is zero at 123 K but was assumed as 10^{-9} $\mathrm{K^{-1}}$ in the calculations to allow for tolerance.
[c]The refractive index for both GaAs and AlGaAs at 150 K was linearly interpolated between known values at 123 and 300 K, and their thermo-optic coefficients assumed constant for consistency.

silicon, GaAs, AlGaAs, and ASTM A229 steel at 123 and 150 K that were used in the calculations. The quantum noise trace was calculated using the pykat/Finesse software package [80–82] for the parameters listed in Table I. All other noise traces were calculated with the GWINC software package [78], subject to the above mentioned modifications.

The detector noise upward of 500 Hz is dominated by quantum noise and a small number of peaks in the suspension thermal noise trace, which are caused by violin modes in the steel wires of the final suspension stage. Targeted damping and data filtering can lessen their impact, as they are quite narrow. Several sources of thermal noise are within close proximity of each other in this region; however, there is sufficient margin to quantum noise to result in minimal impact on detector performance.

Substrate thermoelastic noise, which is a particular concern for raising the ITM temperature, and ITM thermorefractive noise are prominent at low frequencies, but due to their $1/f$ frequency dependence they fall below the coating noises in the sensitivity band. Seismic noise and Newtonian noise are inconsequential at kilohertz frequencies.

For comparison, we also consider an NEMO variant that employs the same tantala/silica mirror coatings used by Advanced LIGO and Advanced Virgo in their first three coordinated observation runs. These coatings have higher thermal noise, but the combined relief of cryogenic temperatures and increased beam size made possible by the larger mirrors is able to lower the coating noise despite the thicker coatings required for the longer wavelength.

In the calculations, we account for a rise in mechanical loss of the coating toward low temperatures [38,83] and the frequency dependence of the tantala loss, as supported by GWINC. For the Young's modulus, Poisson's ratio, specific heat, thermal conductivity, coefficient of thermal expansion, and thermo-optic coefficient of both silica and tantala, we assumed room temperature values. Figure 7 compares the sensitivity that could be obtained if the aLIGO coatings were used compared with the AlGaAs coating case. In this figure only, the coating noise traces and total detector noise for both cases are shown. Other noise traces were counted toward the total noise but have been omitted from the plot, since they are identical in both cases. As can be seen, the noise floor rises only marginally, the majority of which is caused by the higher Brownian noise. The thermo-optic noise of the tantala/silica coatings is roughly 35% lower in the NEMO sensitivity band. The average increase in detector noise between 1 and 2 kHz is about 15%.

As a last step, we test the applicability of the elevated test mass temperature approach to cryogenic broadband detectors. Specifically, we use LIGO Voyager as an example because it served as a starting point for the NEMO concept. It is important that this discussion is understood in the context that Voyager has been optimized for a very different

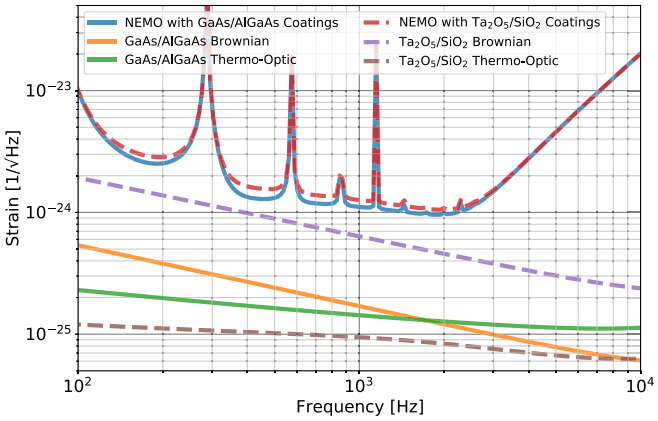

FIG. 7. Comparison of the thermal noise of crystalline AlGaAs coatings and aLIGO-type tantala coatings in the NEMO configuration. The total detector noise traces include noise sources that have been omitted for clarity. The higher Brownian noise of the tantala coatings is primarily caused by their higher mechanical loss.

science case and subject to a larger number of constraints, operation at 123 K being only one of them. We change only this specific aspect without subsequent adjustment of other parameters.

In Voyager, the power absorbed by the mirror is dominated by coating absorption. As a result, a larger-than-budgeted heat load, for example, due to excess coating absorption or increased laser power, would affect ITMs and ETMs to the same degree, commanding an increase of the temperatures of all test masses. In Fig. 8, we show how the instrument noise in Voyager would be affected, assuming other parameters remain unchanged. The noise curves and four exemplar traces of binary coalescence waveforms are shown as unit-less characteristic strain, which is calculated as the square root of the power spectral density multiplied

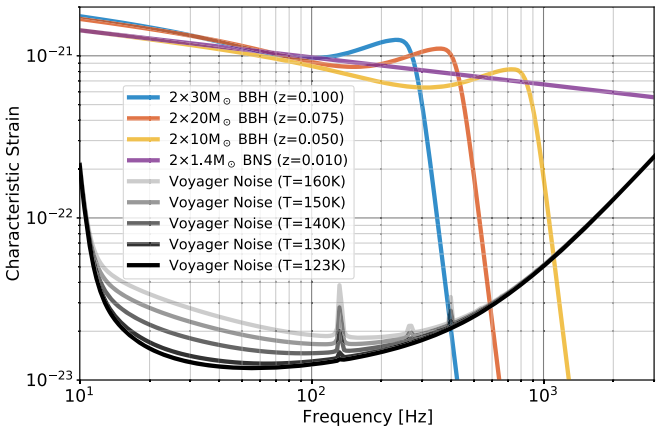

FIG. 8. LIGO Voyager noise at elevated test mass temperatures in characteristic strain units. The traces of four gravitational wave signals through the sensitivity band are shown at typical redshifts. The increased detector noise affects predominantly the inspiral phases.

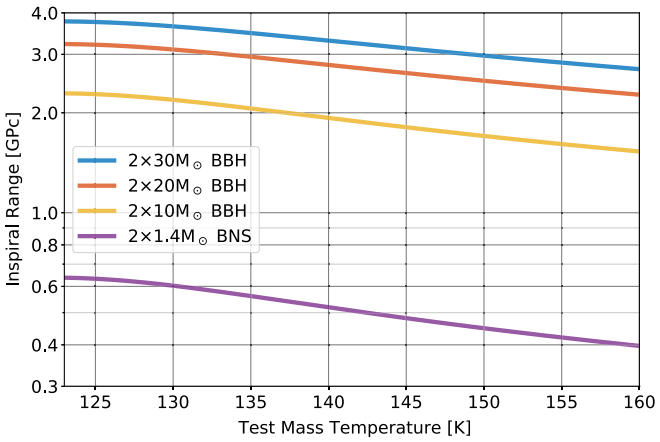

FIG. 9. LIGO Voyager inspiral range vs test mass temperature. The broadband detector is significantly more susceptible to the increased thermal noise of elevated test mass temperatures. The inspiral range was calculated using the GWINC and LALinference software packages.

by the frequency. The frequency domain waveforms were calculated with the lalsimulation package [84] using the IMRPhenomD method [85,86] for the binary black hole merger signals and the TaylorF2 method [87] for the BNS waveform. The sources were assumed to be optimally oriented for maximum signal-to-noise ratio (SNR) in the detector at the indicated redshifts.

The increase in detector noise predominantly affects the inspiral stage, whereas the merger and ringdown phases, particularly for the lighter sources, experience only little impact. This is not all too surprising and reflects the premise behind the development of the NEMO design. We plot in Fig. 9 the corresponding loss in inspiral range for Voyager. Over the same temperatures, NEMO loses less than 1.5% of its BNS range to rising thermal noise, assuming integration of the BNS signals only at frequencies above 500 Hz. While this makes the NEMO science case seem robust to further increases of the ITM temperature, the excess substrate absorption that may suggest such an approach and the accompanying increased scatter loss from thermal lensing was not factored into additional SRC losses and squeezing degradation for the calculation of inspiral range.

Voyager would lose SNR and inspiral range relatively quickly: at 150 K, at roughly double the cooling rate, the range is reduced by 20%–30% compared to 123 K, depending on the source. The increased cooling rate could either be used to compensate a higher coating absorption than 1 ppm, or alternatively to increase the optical power in the interferometer, with benefits for the high frequency sensitivity. The corresponding decrease in shot noise in the black hole merger band may serve as the basis for further response tuning efforts and give access to more elusive source parameters and allow more accurate tests of general relativity.

VIII. CONCLUSION

Next generational gravitational wave detectors with high sensitivity around 2 kHz will reveal the dynamics of the last moments of collapsing binary neutron star systems. In this paper, we gave a detailed description of several key parts of the NEMO concept for a kilohertz-band detector which allows a quantum-noise limited sensitivity at the level of 10^{-24} $\mathrm{Hz}^{-1/2}$ and potentially lower. This sensitivity will allow the full merger and ringdown phase of binary inspirals to be observed. High optical power and quantum squeezing are imperative to achieve this ambitious sensitivity goal. The NEMO detector design was developed to use technology that is largely available or projected to become available within a few years.

The NEMO detector uses cryogenic silicon test masses to reduce thermal noise and reduce the impact of thermal aberrations that result from the required high circulating power. The dominant power handling risk that remains is the impact of thermally induced lenses caused by homogeneous absorption and higher-order aberrations caused by inhomogeneous absorption in the substrates. Theoretical estimates suggest that precise thermal compensation can deal with the homogeneous absorption. More detailed studies are required to understand the likely inhomogeneous absorption issue.

In this paper, we have shown that NEMO can maintain its sensitivity performance and radiatively dissipate the significant power that is deposited in its cryogenic test masses if it operates its ITMs at 150 K.

ACKNOWLEDGMENTS

The authors thank Garrett Cole for information about crystalline coatings and their properties. This work was supported by the Australian Research Council Centre of Excellence for Gravitational Wave Discovery (OzGrav) through Project No. CE170100004.

[1] K. Takami, L. Rezzolla, and L. Baiotti, Phys. Rev. D **91**, 064001 (2015).
[2] P. D. Lasky, Pub. Astron. Soc. Aust. **32**, e034 (2015).
[3] C. Markakis, J. S. Read, M. Shibata, K. Uryū, J. D. E. Creighton, J. L. Friedman, and B. D. Lackey, J. Phys. Conf. Ser. **189**, 012024 (2009).
[4] B. D. Lackey and L. Wade, Phys. Rev. D **91**, 043002 (2015).
[5] K. Ackley *et al.* (OzGrav Collaboration), Pub. Astron. Soc. Aust. **37**, e047 (2020).
[6] H. Miao, H. Yang, and D. Martynov, Phys. Rev. D **98**, 044044 (2018).
[7] D. Martynov, H. Miao, H. Yang, F. H. Vivanco, E. Thrane, R. Smith, P. Lasky, W. E. East, R. Adhikari, A. Bauswein *et al.*, Phys. Rev. D **99**, 102004 (2019).
[8] W. Winkler, K. Danzmann, A. Rüdiger, and R. Schilling, Phys. Rev. A **44**, 7022 (1991).
[9] K. Strain, K. Danzmann, J. Mizuno, P. Nelson, A. Rdiger, R. Schilling, and W. Winkler, Phys. Lett. A **194**, 124 (1994).
[10] H. Wang, C. Blair, M. D. Álvarez, A. Brooks, M. F. Kasprzack, J. Ramette, P. M. Meyers, S. Kaufer, B. O'Reilly, C. M. Mow-Lowry *et al.*, Classical Quantum Gravity **34**, 115001 (2017).
[11] R. C. Lawrence, Ph. D. thesis, Massachusetts Institute of Technology, 2003.
[12] A. Buikema, C. Cahillane, G. L. Mansell, C. D. Blair, R. Abbott, C. Adams, R. X. Adhikari, A. Ananyeva, S. Appert, K. Arai *et al.*, Phys. Rev. D **102**, 062003 (2020).
[13] R. X. Adhikari, K. Arai, A. F. Brooks, C. Wipf, O. Aguiar, P. Altin, B. Barr, L. Barsotti, R. Bassiri, A. Bell *et al.*, Classical Quantum Gravity **37**, 165003 (2020).
[14] M. Punturo *et al.*, Classical Quantum Gravity **27**, 084007 (2010).
[15] Y. Aso, Y. Michimura, K. Somiya, M. Ando, O. Miyakawa, T. Sekiguchi, D. Tatsumi, and H. Yamamoto (The KAGRA Collaboration), Phys. Rev. D **88**, 043007 (2013).
[16] F. Matichard, B. Lantz, R. Mittleman, K. Mason, J. Kissel, B. Abbott, S. Biscans, J. McIver, R. Abbott, S. Abbott *et al.*, Classical Quantum Gravity **32**, 185003 (2015).
[17] S. M. Aston, M. A. Barton, A. S. Bell, N. Beveridge, B. Bland, A. J. Brummitt, G. Cagnoli, C. A. Cantley, L. Carbone, A. V. Cumming *et al.*, Classical Quantum Gravity **29**, 235004 (2012).
[18] The VIRGO Collaboration (presented by Braccini), Classical Quantum Gravity **19**, 1623 (2002).
[19] F. Travasso on behalf of the VIRGO Collaboration, J. Phys. Conf. Ser. **957**, 012012 (2018).
[20] J. Aasi, B. P. Abbott, R. Abbott, T. Abbott, M. R. Abernathy, K. Ackley *et al.*, Classical Quantum Gravity **32**, 074001 (2015).
[21] F. Acernese, M. Agathos, K. Agatsuma, D. Aisa, N. Allemandou, A. Allocca *et al.*, Classical Quantum Gravity **32**, 024001 (2015).
[22] W. Lin and H. Huff, in *Handbook of Semiconductor Manufacturing Technology*, edited by R. Doering and Y. Nishi (CRC Press, Boca Raton, 2008), Chap. 8.
[23] E. Oelker, T. Isogai, J. Miller, M. Tse, L. Barsotti, N. Mavalvala, and M. Evans, Phys. Rev. Lett. **116**, 041102 (2016).
[24] L. McCuller, C. Whittle, D. Ganapathy, K. Komori, M. Tse, A. Fernandez-Galiana, L. Barsotti, P. Fritschel, M. MacInnis, F. Matichard *et al.*, Phys. Rev. Lett. **124**, 171102 (2020).
[25] M. J. Yap, P. Altin, T. G. McRae, B. J. J. Slagmolen, R. L. Ward, and D. E. McClelland, Nat. Photonics **14**, 223 (2020).
[26] D. E. McClelland, Aust. J. Phys. **48**, 953 (1995).
[27] H. Miao, H. Yang, R. X. Adhikari, and Y. Chen, Classical Quantum Gravity **31**, 165010 (2014).
[28] V. B. Adya, M. J. Yap, D. Tyr, T. G. McRae, P. A. Altin, L. K. Sarre, M. Meijerink, N. Kijbunchoo, B. J. J. Slagmolen, R. L. Ward *et al.*, Classical Quantum Gravity **37**, 07LT02 (2020).
[29] M. Evans, S. Gras, P. Fritschel, J. Miller, L. Barsotti, D. Martynov, A. Brooks, D. Coyne, R. Abbott, R. X. Adhikari *et al.*, Phys. Rev. Lett. **114**, 161102 (2015).
[30] J. Pan *et al.* (to be published).
[31] T. G. Euser and W. L. Vos, J. Appl. Phys. **97**, 043102 (2005).
[32] J. Degallaix, R. Flaminio, D. Forest, M. Granata, C. Michel, L. Pinard, T. Bertrand, and G. Cagnoli, Opt. Lett. **38**, 2047 (2013).
[33] M. Granata, A. Amato, L. Balzarini, M. Canepa, J. Degallaix, D. Forest, V. Dolique, L. Mereni, C. Michel, L. Pinard *et al.*, Classical Quantum Gravity **37**, 095004 (2020).
[34] S. Gras and M. Evans, Phys. Rev. D **98**, 122001 (2018).
[35] M. Principe, I. M. Pinto, V. Pierro, R. DeSalvo, I. Taurasi, A. E. Villar, E. D. Black, K. G. Libbrecht, C. Michel, N. Morgado *et al.*, Phys. Rev. D **91**, 022005 (2015).
[36] P. G. Murray, I. W. Martin, K. Craig, J. Hough, R. Robie, S. Rowan, M. R. Abernathy, T. Pershing, and S. Penn, Phys. Rev. D **92**, 062001 (2015).
[37] D. T. Pierce and W. E. Spicer, Phys. Rev. B **5**, 3017 (1972).
[38] I. W. Martin, R. Nawrodt, K. Craig, C. Schwarz, R. Bassiri, G. Harry, J. Hough, S. Penn, S. Reid, R. Robie *et al.*, Classical Quantum Gravity **31**, 035019 (2014).
[39] L.-C. Kuo, H.-W. Pan, C.-L. Chang, and S. Chao, Opt. Lett. **44**, 247 (2019).
[40] J. Steinlechner, I. W. Martin, A. S. Bell, J. Hough, M. Fletcher, P. G. Murray, R. Robie, S. Rowan, and R. Schnabel, Phys. Rev. Lett. **120**, 263602 (2018).
[41] R. Birney, J. Steinlechner, Z. Tornasi, S. MacFoy, D. Vine, A. S. Bell, D. Gibson, J. Hough, S. Rowan, P. Sortais *et al.*, Phys. Rev. Lett. **121**, 191101 (2018).
[42] G. D. Cole, S. Gröblacher, K. Gugler, S. Gigan, and M. Aspelmeyer, Appl. Phys. Lett. **92**, 261108 (2008).
[43] G. D. Cole, W. Zhang, M. J. Martin, J. Ye, and M. Aspelmeyer, Nat. Photonics **7**, 644 (2013).
[44] S. D. Penn, M. M. Kinley-Hanlon, I. A. O. MacMillan, P. Heu, D. Follman, C. Deutsch, G. D. Cole, and G. M. Harry, J. Opt. Soc. Am. B **36**, C15 (2019).
[45] P. R. Saulson, Phys. Rev. D **42**, 2437 (1990).
[46] N. Robertson and LIGO Scientific Collaboration, HAM large triple suspension (HLTS) final design document, LIGO, Technical Report No. LIGO-T1000012, 2010, https://dcc.ligo.org/LIGO-T1000012/public.
[47] M. V. Plissi and LIGO Scientific Collaboration, Cantilever blade analysis for Advanced LIGO, LIGO, Technical Report No. LIGO-T030107, 2003, https://dcc.ligo.org/LIGO-T030107/public.

[48] G. González, Classical Quantum Gravity **17**, 4409 (2000).
[49] G. Cagnoli, J. Hough, D. DeBra, M. Fejer, E. Gustafson, S. Rowan, and V. Mitrofanov, Phys. Lett. A **272**, 39 (2000).
[50] V. B. Braginsky, V. P. Mitrofanov, and O. A. Okhrimenko, Phys. Lett. A **175**, 82 (1993).
[51] G. I. González and P. R. Saulson, J. Acoust. Soc. Am. **96**, 207 (1994).
[52] A. V. Cumming, L. Cunningham, G. D. Hammond, K. Haughian, J. Hough, S. Kroker, I. W. Martin, R. Nawrodt, S. Rowan, C. Schwarz *et al.*, Classical Quantum Gravity **31**, 025017 (2014).
[53] S. Rowan, R. L. Byer, M. M. Fejer, R. K. Route, G. Cagnoli, D. R. Crooks, J. Hough, P. H. Sneddon, and W. Winkler, in *Gravitational-Wave Detection*, edited by P. Saulson and A. M. Cruise, International Society for Optics and Photonics, Vol. 4856 (SPIE, 2003), pp. 292–297, https://doi.org/10.1117/12.459019.
[54] B. P. Abbott, R. Abbott, T. D. Abbott, M. R. Abernathy, F. Acernese, K. Ackley *et al.* (LIGO Scientific and Virgo Collaborations), Phys. Rev. Lett. **116**, 061102 (2016).
[55] Y. Levin, Phys. Rev. D **57**, 659 (1998).
[56] V. Braginsky, M. Gorodetsky, and S. Vyatchanin, Phys. Lett. A **264**, 1 (1999).
[57] G. M. Harry, A. M. Gretarsson, P. R. Saulson, S. E. Kittelberger, S. D. Penn, W. J. Startin, S. Rowan, M. M. Fejer, D. R. M. Crooks, G. Cagnoli *et al.*, Classical Quantum Gravity **19**, 897 (2002).
[58] G. M. Harry, H. Armandula, E. Black, D. R. M. Crooks, G. Cagnoli, J. Hough, P. Murray, S. Reid, S. Rowan, P. Sneddon *et al.*, Appl. Opt. **45**, 1569 (2006).
[59] T. Hong, H. Yang, E. K. Gustafson, R. X. Adhikari, and Y. Chen, Phys. Rev. D **87**, 082001 (2013).
[60] M. Evans, S. Ballmer, M. Fejer, P. Fritschel, G. Harry, and G. Ogin, Phys. Rev. D **78**, 102003 (2008).
[61] S. W. Ballmer, Phys. Rev. D **91**, 023010 (2015).
[62] G. Cagnoli and P. A. Willems, Phys. Rev. B **65**, 174111 (2002).
[63] D. Heinert, A. Bell, G. Cagnoli, J. Degallaix, G. Gemme, S. Hild, J. Hough, H. Luck, I. W. Martin, S. Rowan *et al.*, Free carrier driven noise in transmissive semiconductor optics, LIGO, Internal Document No. LIGO-P1400084, 2014, LIGO-1400084.
[64] F. Bruns, S. P. Vyatchanin, J. Dickmann, R. Glaser, D. Heinert, R. Nawrodt, and S. Kroker, Phys. Rev. D **102**, 022006 (2020).
[65] P. D. Desai, J. Phys. Chem. Ref. Data **15**, 967 (1986).
[66] C. Y. Ho, R. W. Powell, and P. E. Liley, J. Phys. Chem. Ref. Data **1**, 279 (1972).
[67] C. J. Glassbrenner and G. A. Slack, Phys. Rev. **134**, A1058 (1964).
[68] C. A. Swenson, J. Phys. Chem. Ref. Data **12**, 179 (1983).
[69] B. J. Frey, D. B. Leviton, and T. J. Madison, in *Optomechanical Technologies for Astronomy*, edited by E. Atad-Ettedgui, J. Antebi, and D. Lemke, International Society for Optics and Photonics, Vol. 6273 (SPIE, 2006), pp. 790–799, https://doi.org/10.1117/12.672850.
[70] H. J. McSkimin, J. Appl. Phys. **24**, 988 (1953).
[71] A. Zimmer, R. Nawrodt, D. Heinert, C. Schwarz, M. Hudl, T. Koettig, W. Vodel, A. Tnnermann, and P. Seidel, J. Phys. Conf. Ser. **92**, 012095 (2007).
[72] G. D. Cole (private communication).
[73] T. Chalermsongsak, E. D. Hall, G. D. Cole, D. Follman, F. Seifert, K. Arai, E. K. Gustafson, J. R. Smith, M. Aspelmeyer, and R. X. Adhikari, Metrologia **53**, 860 (2016).
[74] K. Asakawa, Adv. Mater. **5**, 228 (1993).
[75] S. Tiwari, in *Compound Semiconductor Device Physics*, edited by S. Tiwari (Academic Press, Boston, 1992), pp. 7–104, ISBN 978-0-12-691740-6.
[76] S. I. Novikova, Sov. Phys. Solid State **3**, 129 (1961).
[77] H.-M. Kagaya and T. Soma, Solid State Commun. **62**, 707 (1987).
[78] Python Gravitational Wave Interferometer Noise Calculator, https://git.ligo.org/gwinc/pygwinc, latest considered commit: f9d5d5b8, 2020-07-08.
[79] G. Vajente, M. Fazio, L. Yang, A. Gupta, A. Ananyeva, G. Billinsley, and C. S. Menoni, Phys. Rev. D **101**, 042004 (2020).
[80] A. Freise, G. Heinzel, H. Lück, R. Schilling, B. Willke, and K. Danzmann, Classical Quantum Gravity **21**, S1067 (2004); finesse is available at http://www.gwoptics.org/finesse.,
[81] D. D. Brown and A. Freise, Finesse (2014), https://doi.org/10.5281/zenodo.821363.
[82] D. D. Brown, P. Jones, S. Rowlinson, A. Freise, S. Leavey, A. C. Green, and D. Toyra, Pykat: Python package for modelling precision optical interferometers, arXiv:2004.06270.
[83] I. W. Martin, R. Bassiri, R. Nawrodt, M. M. Fejer, A. Gretarsson, E. Gustafson, G. Harry, J. Hough, I. MacLaren, S. Penn *et al.*, Classical Quantum Gravity **27**, 225020 (2010).
[84] LIGO Scientific Collaboration, LIGO Algorithm Library—LALSuite, free software (GPL) (2018), https://doi.org/10.7935/GT1W-FZ16.
[85] S. Husa, S. Khan, M. Hannam, M. Pürrer, F. Ohme, X. J. Forteza, and A. Bohé, Phys. Rev. D **93**, 044006 (2016).
[86] S. Khan, S. Husa, M. Hannam, F. Ohme, M. Pürrer, X. J. Forteza, and A. Bohé, Phys. Rev. D **93**, 044007 (2016).
[87] A. Buonanno, B. R. Iyer, E. Ochsner, Y. Pan, and B. S. Sathyaprakash, Phys. Rev. D **80**, 084043 (2009).